Am J Physiol Cell Physiol 310: C337–C347, 2016.
First published November 25, 2015; doi:10.1152/ajpcell.00234.2015.

CALL FOR PAPERS | *Cell Signaling: Proteins, Pathways and Mechanisms*

Modeling analysis of inositol 1,4,5-trisphosphate receptor-mediated Ca^{2+} mobilization under the control of glucagon-like peptide-1 in mouse pancreatic β-cells

Yukari Takeda,[1] Takao Shimayoshi,[2] George G. Holz,[3] and Akinori Noma[1]

[1]*Department of Bioinformatics, College of Life Sciences, Ritsumeikan University, Kusatsu City, Japan;* [2]*Department of Systems Science, Kyoto University, Kyoto, Japan; and* [3]*Departments of Medicine and Pharmacology, SUNY Upstate Medical University, Syracuse, New York*

Submitted 10 August 2015; accepted in final form 19 November 2015

Takeda Y, Shimayoshi T, Holz GG, Noma A. Modeling analysis of inositol 1,4,5-trisphosphate receptor-mediated Ca^{2+} mobilization under the control of glucagon-like peptide-1 in mouse pancreatic β-cells. *Am J Physiol Cell Physiol* 310: C337–C347, 2016. First published November 25, 2015; doi:10.1152/ajpcell.00234.2015.—Glucagon-like peptide-1 (GLP-1) is an intestinally derived blood glucose-lowering hormone that potentiates glucose-stimulated insulin secretion from pancreatic β-cells. The secretagogue action of GLP-1 is explained, at least in part, by its ability to stimulate cAMP production so that cAMP may facilitate the release of Ca^{2+} from inositol trisphosphate receptor (IP_3R)-regulated Ca^{2+} stores. However, a quantitative model has yet to be provided that explains the molecular mechanisms and dynamic processes linking GLP-1-stimulated cAMP production to Ca^{2+} mobilization. Here, we performed simulation studies to investigate how GLP-1 alters the abilities of Ca^{2+} and IP_3 to act as coagonists at IP_3R Ca^{2+} release channels. A new dynamic model was constructed based on the Kaftan model, which demonstrates dual steady-state allosteric regulation of the IP_3R by Ca^{2+} and IP_3. Data obtained from β-cells were then analyzed to understand how GLP-1 facilitates IP_3R-mediated Ca^{2+} mobilization when UV flash photolysis is used to uncage Ca^{2+} and IP_3 intracellularly. When the dynamic model for IP_3R activation was incorporated into a minimal cell model, the Ca^{2+} transients and oscillations induced by GLP-1 were successfully reconstructed. Simulation studies indicated that transient and oscillatory responses to GLP-1 were produced by sequential positive and negative feedback regulation due to fast activation and slow inhibition of the IP_3R by Ca^{2+}. The slow rate of Ca^{2+}-dependent inhibition was revealed to provide a remarkable contribution to the time course of the decay of cytosolic Ca^{2+} transients. It also served to drive and pace Ca^{2+} oscillations that are significant when evaluating how GLP-1 stimulates insulin secretion.

inositol 1,4,5-trisphosphate; glucagon-like peptide-1; Ca^{2+} mobilization; model stimulation

PANCREATIC β-CELLS PLAY a central role in the control of blood glucose homeostasis by generating bursts of action potentials when levels of blood glucose rise after a meal. This rhythmic bursting activity is accompanied by oscillations of intracellular Ca^{2+} concentration ($[Ca^{2+}]_i$) that induce pulsatile insulin secretion (2; 17, 38). Glucagon-like peptide-1 (GLP-1) is also an insulin secretagogue (30), and it activates G protein-coupled receptors (GPCRs) on β-cells to stimulate cAMP production so that cAMP signaling pathways may facilitate the inositol trisphosphate receptor (IP_3R)-dependent release of Ca^{2+} from endoplasmic reticulum (ER) Ca^{2+} stores (12, 13, 20, 24–27, 32, 37). This IP_3R-dependent ER Ca^{2+} release serves as a direct stimulus for insulin secretion (26), and it occurs when β-cells are simultaneously exposed to glucose and GLP-1 so that levels of intracellular IP_3, Ca^{2+}, and cAMP are elevated in concert (19, 31). In the present study, we report mathematical simulation studies that reveal how β-cell IP_3Rs act as molecular coincidence detectors so that their gating function is regulated not only by IP_3 and Ca^{2+} but also by cAMP.

Studies using microsomal vesicles containing the IP_3R derived from rat brain synaptosomes (14) provide a conceptual framework with which to evaluate how such coordinate regulation of ER Ca^{2+} mobilization is achieved. These studies indicate a positive feedback action of Ca^{2+} to potentiate IP_3-induced Ca^{2+} release that is measurable in living cells as a transient increase of $[Ca^{2+}]_i$. A subsequent decay of the Ca^{2+} transient is explained by Ca^{2+}-dependent inhibition (or possibly inactivation) of the IP_3R rather than depletion of Ca^{2+} stores. Collectively, these findings indicate that sequential positive and negative feedback regulation of the IP_3R by Ca^{2+} determines the time course of Ca^{2+} transients as well as Ca^{2+} oscillations. Still, it remains uncertain how Ca^{2+}, IP_3, and cAMP functionally interact to control IP_3R activity.

Among the three subtypes of IP_3 receptors (IP_3R1, IP_3R2, and IP_3R3) identified so far, it is IP_3R1 that is predominantly expressed in mouse β-cells (29). The activity of IP_3R1 is determined by the occupancy of two major IP_3 binding sites; one with high affinity for IP_3, and another with low affinity ($K_d = 0.05 \sim 1.78$ and 10 μM, respectively). Ca^{2+} acts as a coagonist, and the bell-shaped bimodal regulation of the steady-state channel open probability (P_o) by cytosolic Ca^{2+} is explained by two Ca^{2+} binding sites: one is for channel activation ($K_d = 0.8$ μM) and the other is for channel inhibition (K_d not yet determined) (6, 8, 22, 23, 35, 36, 40, 45). However, one limitation of earlier mathematical models of IP_3R1 regulation is that some models described a single high-affinity IP_3 binding site, usually omitting the low-affinity IP_3 binding site (9, 10, 16). Since these models predicted saturated channel activity at a basal cytosolic concentration of IP_3 concentration ($[IP_3]$; ~2 μM; Refs. 4, 21), they were not suitable for analysis of IP_3R1 channel activity at physiologi-

---

Address for reprint requests and other correspondence: Y. Takeda, 1-1-1 Nojihigashi, Kusatsu, Shiga 525-8577, Japan (e-mail: yukari@fc.ritsumei.ac.jp).

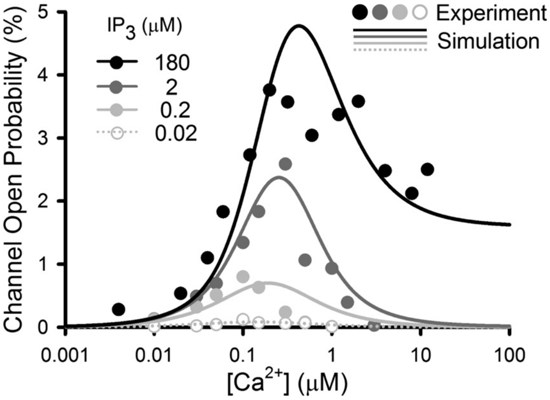

Fig. 1. Open probabilities of the inositol trisphosphate receptor (IP$_3$R) as a function of the Ca^{2+} concentration. Experimentally measured open probabilities of the IP$_3$R were prepared from canine cerebellar endoplasmic reticulum (ER) microsomes (where type 1 receptors are exclusively expressed) and studied in planar lipid bilayers. Data are plotted as filled circles as a function of the Ca^{2+} concentration. Ca^{2+}-dependent results of the simulations obtained at different IP$_3$ concentrations are indicated in the corresponding colors [data are modified from Kaftan et al. (23), see MATERIALS AND METHODS]. Simulation results (solid and dotted lines) are superimposed upon experimental results.

cally relevant higher concentrations of IP$_3$. A significant improvement that allowed accurate simulation of IP$_3$R1 channel activity was the steady-state IP$_3$R1 model of Kaftan et al. (23) that considered both high- and low-affinity IP$_3$ binding sites, as well as two Ca^{2+}-binding sites. Using experimental approaches, Kaftan et al. (23), demonstrated that Ca^{2+}-dependent channel activity increased as levels of [IP$_3$] (0.02∼180 μM) also increased. By taking into account both high- and low-affinity IP$_3$ binding sites, the model of Kaftan et al. (23) successfully simulated IP$_3$R1 channel activity over a wide range of IP$_3$ and [Ca^{2+}].

In the mathematical simulation studies reported here, a new dynamic model of IP$_3$R Ca^{2+} channel activity is constructed based on the steady-state IP$_3$R1 model originally developed by Kaftan et al. (23). The model accurately reconstructs the steady-state open probability of the IP$_3$R over a wide range of [IP$_3$] and [Ca^{2+}]. Results derived from the present theoretical studies indicate that for β-cells in which the activities IP$_3$R and sarco(endo)plasmic reticulum Ca^{2+}-ATPase (SERCA) are enhanced through cAMP-dependent protein kinase (PKA) activation, the resultant transient changes of [Ca^{2+}]$_i$ are produced by sequential positive and negative feedback regulation due to fast activation and slow inhibition of the IP$_3$R by Ca^{2+}. Interestingly, the model exhibited the ability to produce oscillatory Ca^{2+} mobilization when intracellular Ca^{2+} content was elevated. Remarkably, we find that the rate of Ca^{2+}-dependent inhibition is critically important to the time course of the decay of the Ca^{2+} transient, and it also determines the frequency of Ca^{2+} oscillations.

MATERIALS AND METHODS

A dynamic IP$_3$R1 model was first developed on the basis of the model of Kaftan et al (23), which accurately reproduces steady-state activities of the channel that are known to be allosterically regulated by both [Ca^{2+}] and [IP$_3$] (Fig. 1). Ca^{2+} transients and oscillations were then reconstructed in a minimal cell model, as fully described below. Simulation studies and mathematical analyses were subsequently applied to investigate quantitative mechanisms underlying the IP$_3$R-mediated Ca^{2+}-release events in pancreatic β-cells. Model development and simulation-based analyses were both performed on Microsoft Visual Studio, unless otherwise indicated. Time integration of the differential equations was conducted using the Euler method with a time step of 1 ms.

Modeling the steady-state open probability of the IP$_3$R at different agonist concentrations. On the basis of the model of Kaftan et al. (23), the steady-state open probabilities of the IP$_3$R over a wide range of [IP$_3$] and [Ca^{2+}] (Fig. 1) were reconstructed to determine dissociation constants (K_d) for agonist binding sites. IP$_3$R forms a complex comprised of four subunits. Kaftan et al. (23) assumed that each subunit in the tetrameric complex contains two IP$_3$ binding sites (IP$_3$H: higher affinity site; and IP$_3$L: lower affinity site) and two Ca^{2+} binding sites (CaA: activation site; and CaI: inhibition site) according to experimental findings (6, 8, 22, 23, 35, 36, 40, 45). Since Ca^{2+} inhibits IP$_3$ binding to the channel due to an increase in the dissociation constant (K_d) of the IP$_3$ binding sites (22), Kaftan et al. assumed that the steady-state probability of IP$_3$ binding at IP$_3$H (P_{IP3Hip3}) was determined by two distinct K_d values (K_{dIP3H}; K_d when Ca^{2+} was not bound to CaI, and K_{dIP3Hca}; K_d when Ca^{2+} was bound to CaI) depending on the occupancy of the CaI site (*Eq. 1*). In contrast, the steady-state probabilities for IP$_3$ bound to IP$_3$L (P_{IP3Lip3}) as well as Ca^{2+} bound to CaA (P_{CaAca}) and CaI (P_{CaIca}) were simply calculated by *Eqs. 2–4* with corresponding dissociation constants (K_{dIP3L}, K_{dCaA}, and K_{dCaI}, respectively).

$$P_{\mathrm{IP3Hip3}} = \frac{1}{1 + \dfrac{P_{\mathrm{CaI}} \cdot K_{\mathrm{dIP3H}} + P_{\mathrm{CaIca}} \cdot K_{\mathrm{dIP3Hca}}}{[\mathrm{IP_3}]}} \tag{1}$$

$$P_{\mathrm{IP3Lip3}} = \frac{1}{1 + \dfrac{K_{\mathrm{dIP3L}}}{[\mathrm{IP_3}]}} \tag{2}$$

$$P_{\mathrm{CaAca}} = \frac{1}{1 + \dfrac{K_{\mathrm{dCaA}}}{[\mathrm{Ca}]}} \tag{3}$$

$$P_{\mathrm{CaIca}} = \frac{1}{1 + \dfrac{K_{\mathrm{dCaI}}}{[\mathrm{Ca}]}} \tag{4}$$

There are a total of 16 possible states of each monomer associated with every combination of agonist binding. Kaftan et al. (23) assumed that the overall single channel P_o of the tetrameric complex is determined by multiple combinations of agonist binding states of each subunit. The affinities for each agonist binding site in Kaftan et al. was estimated by model fitting to the experimental data for values of P_o over a wide range of [IP$_3$] and [Ca^{2+}]. The Ca^{2+}-dependent P_o curve obtained with a low ATP concentration (0.5 mM), however, was shown to shift to the left as [ATP] increased to a physiological concentration (∼5 mM; Ref. 15). This effect of ATP is apparent when IP$_3$R activity is measured with higher [IP$_3$] (>10 μM) but not at basal levels of [IP$_3$] (∼2 μM; Refs. 4, 21) (3). In the study reported here, K_{dIP3H}, K_{dIP3Hca}, K_{dIP3L}, K_{dCaA}, and K_{dCaI} were thus reevaluated by taking into account the ATP effect in which the Ca^{2+}-dependent P_o curve obtained with 180 μM IP$_3$ was left-shifted (Fig. 1). However, other experimental data with lower [IP$_3$] remained unmodified. All assumptions made for the steady-state IP$_3$R model in Kaftan et al. were adopted after reevaluating effects of ATP for the current model study. K_d values for each agonist binding site as well as P_i values [in Kaftan et al. (23)] were estimated by model fitting of the reevaluated data and are listed in Table 1.

Modeling dynamic properties of the IP$_3$R. On the bases of steady-state properties of the IP$_3$R, a new dynamic model was constructed. Key model parameter sets of the dynamic IP$_3$R model were estimated

Table 1. *Parameter sets for the steady-state IP$_3$R model*

Parameters	Experiments	Kaftan Model	Present Model
K_{dIP3H}	0.04–0.31 μM (22, 23, 36, 45)	0.3 μM	0.1 μM
K_{dIP3HCa}	0.54–1.78 μM (22, 23, 36)	1.5 μM	0.4 μM
K_{dIP3L}	~10 μM (23)	10 μM	800 μM
K_{dCaA}	0.8 μM (40)	0.03 μM	0.27 μM
K_{dCaI}		1.0 μM	0.27 μM
P_1		10 E-11	0.01
P_2		0.06	0.03
P_3		0.04	0.34
P_4		Not indicated	0.98

Parameter sets for the steady-state inositol trisphosphate receptor (IP$_3$R) model, as estimated by a comparison of the theoretical study of Kaftan et al. (23) and experimental findings (22, 23, 36, 40, 45). See text for definitions.

by accurately simulating the changes of [Ca^{2+}] during the time course of Ca^{2+} transients that result from Ca^{2+}-induced Ca^{2+} release (CICR) in mouse β-cells (25). To reproduce Ca^{2+} transients and oscillations generated in β-cells, the equilibrium equations for binding of Ca^{2+} to CaA (*Eq. 3*) and CaI (*Eq. 4*) were replaced by time-dependent processes (*Eqs. 5* and *6*). Chronological changes in P_{CaAca} and P_{CaIca} of the IP$_3$R were thus determined by time-based integration of *Eqs. 5* and *6* where α and β represent overall rates for Ca^{2+} association and dissociation with respective binding sites followed by subsequent activation or inhibition of the channel.

$$\frac{\mathrm{d}P_{\mathrm{CaAca}}}{\mathrm{d}t} = \alpha_{\mathrm{CaA}} \cdot P_{\mathrm{CaA}} \cdot \left[\mathrm{Ca}^{2+}\right]_{\mathrm{nrs}} - \beta_{\mathrm{CaA}} \cdot P_{\mathrm{CaAca}} \tag{5}$$

$$\frac{\mathrm{d}P_{\mathrm{CaIca}}}{\mathrm{d}t} = \alpha_{\mathrm{CaI}} \cdot P_{\mathrm{CaI}} \cdot \left[\mathrm{Ca}^{2+}\right]_{\mathrm{nrs}} - \beta_{\mathrm{CaI}} \cdot P_{\mathrm{CaIca}} \tag{6}$$

The rate constants α_{CaA}, β_{CaA}, α_{CaI}, and β_{CaI} (Table 2) were estimated by reproducing Ca^{2+}-induced Ca^{2+} release (Fig. 3) in a minimal β-cell model (Fig. 2), which is described below. Regulation of the IP$_3$R due to binding of IP$_3$, on the other hand, was approximated by an instantaneous equilibrium (see *Eqs. 1* and *2*) for simplicity.

Table 2. *Best fit parameter sets for reproducing the transient Ca^{2+} response measured in response to UV flash photolysis*

Parameters	Estimated Values
α_{CaA}	6 mM^{-1}·ms^{-1}
β_{CaA}	1.62 E-3 ms^{-1}
α_{CaI}	1.5 E-2 mM^{-1}·ms^{-1}
β_{CaI}	4.05 E-6 ms^{-1}
vol$_{\mathrm{blk}}$	756.27 fl
vol$_{\mathrm{ER}}$	280.0 fl
vol$_{\mathrm{nrs}}$	7.73 fl
f_{i}	0.01
f_{ER}	0.025
P_{IP3R} (control)	13.65 fl/ms
P_{IP3R} (stimulated)	174.72 fl/ms
P_{ERleak}	0.24 fl/ms
P_{SERCA} (control)	0.0691 amol/ms
P_{SERCA} (stimulated)	0.23 amol/ms
P_{nrsblk}	817.31 fl/ms
P_{mleak}	6.0 fl/ms

Best fit parameter sets for reproducing the transient Ca^{2+} response (Ca^{2+}-induced Ca^{2+} release) measured in response to UV flash photolysis (see arrows in Fig. 3) for mouse β-cells loaded with caged Ca^{2+} (NP-EGTA-AM) under conditions in which cells are either prestimulated or not stimulated with forskolin (25). See text for definitions.

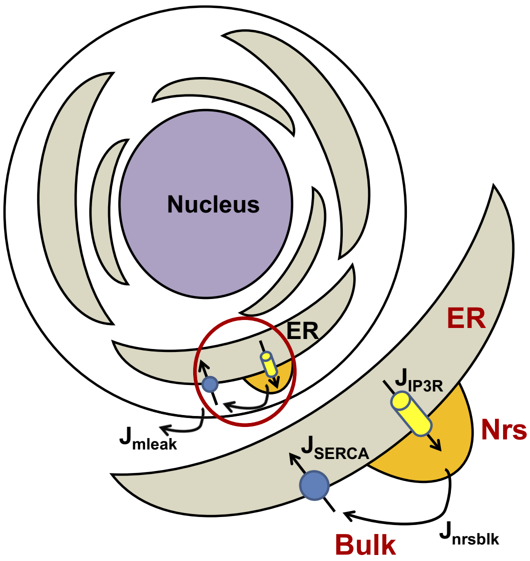

Fig. 2. Schematic diagram describing Ca^{2+} fluxes and Ca^{2+} compartments in the minimal cell model. Ca^{2+} fluxes through the IP$_3$R (J_{IP3R}) and sarco(endo)plasmic reticulum Ca^{2+}-ATPase (SERCA) (J_{SERCA}), as well as Ca^{2+} diffusion from Ca^{2+} microdomains ("nrs") to the bulk ("blk") cytosolic compartment (J_{nrsblk}), are indicated as red circles within a simplified cellular model, and are expanded below. Membrane Ca^{2+} leak (J_{mleak}) was also included. Colors for Ca^{2+} compartments: luminal side of the ER, "nrs" microdomain site, and "blk" cytosolic space are indicated as filled beige, orange, and white, respectively.

Development of the minimal cell model. Schematic illustration of the mouse β-cell minimal cell model is shown in Fig. 2. The model consists of multiple ER Ca^{2+} compartments that contain IP$_3$Rs and SERCA pumps, as a minimum number of functional units for ER Ca^{2+} handling. Net membrane Ca^{2+} flux that signifies plasma membrane Ca^{2+} removal during the Ca^{2+}-induced Ca^{2+} transient (Fig. 3*A*) is described as in J_{mleak} (amol/ms, *Eq. 7*), and Ca^{2+} flux across nuclear membrane was removed for simplicity. The resting [Ca^{2+}]$_{\mathrm{blk}}$ was equilibrated at 0.0001 mM ([Ca^{2+}]$_{\mathrm{rest}}$) by J_{mleak} (*Eq. 7*).

$$J_{\mathrm{mleak}} = P_{\mathrm{mleak}} \cdot \left(\left[\mathrm{Ca}^{2+}\right]_{\mathrm{rest}} - \left[\mathrm{Ca}^{2+}\right]_{\mathrm{blk}}\right) \tag{7}$$

Steep gradients in cytosolic Ca^{2+} concentration are expected near the Ca^{2+} releasing site (nrs). For simplicity, the histological and functional composition of the Ca^{2+} releasing unit for every IP$_3$R was assumed to be uniform throughout the cell. Thus a single compartment containing ER, nrs, and the bulk cytosolic space was implemented for the minimal cell model. Volumes for nrs (vol$_{\mathrm{nrs}}$) are indicated in Table 2, along with ER volume (vol$_{\mathrm{ER}}$) and cytosolic bulk volume (vol$_{\mathrm{blk}}$), as determined on the basis of ultrastructural morphometry (11).

Whole cell molar flux of Ca^{2+} through the IP$_3$R (J_{IP3R}) was defined by *Eq.8*, where P_{o} is the open probability, determined by [Ca^{2+}]$_{\mathrm{nrs}}$.

$$J_{\mathrm{IP3R}} = P_{\mathrm{IP3R}} \cdot P_{\mathrm{o}} \cdot \left(\left[\mathrm{Ca}^{2+}\right]_{\mathrm{ER}} - \left[\mathrm{Ca}^{2+}\right]_{\mathrm{nrs}}\right) \tag{8}$$

Background Ca^{2+} conductivity through the ER membrane (5) was described by *Eq. 9*.

$$J_{\mathrm{ERleak}} = P_{\mathrm{ERleak}} \cdot \left(\left[\mathrm{Ca}^{2+}\right]_{\mathrm{ER}} - \left[\mathrm{Ca}^{2+}\right]_{\mathrm{nrs}}\right) \tag{9}$$

Diffusion of Ca^{2+} from the nrs to blk space, J_{nrsblk}, was assumed as in *Eq. 10*.

$$J_{\mathrm{nrsblk}} = P_{\mathrm{nrsblk}} \cdot \left(\left[\mathrm{Ca}^{2+}\right]_{\mathrm{nrs}} - \left[\mathrm{Ca}^{2+}\right]_{\mathrm{blk}}\right) \tag{10}$$

P_{IP3R}, P_{ERleak}, and P_{nrsblk} in *Eqs. 8–10* as well as P_{mleak} in *Eq. 7* represent conductivities of corresponding Ca^{2+} fluxes with units of fl/ms. Finally, uptake of [Ca^{2+}]$_{\mathrm{blk}}$ by ER through the SERCA pump (J_{SERCA}) was described by *Eq. 11*, where K_{d} = 0.0002 mM, and Hill

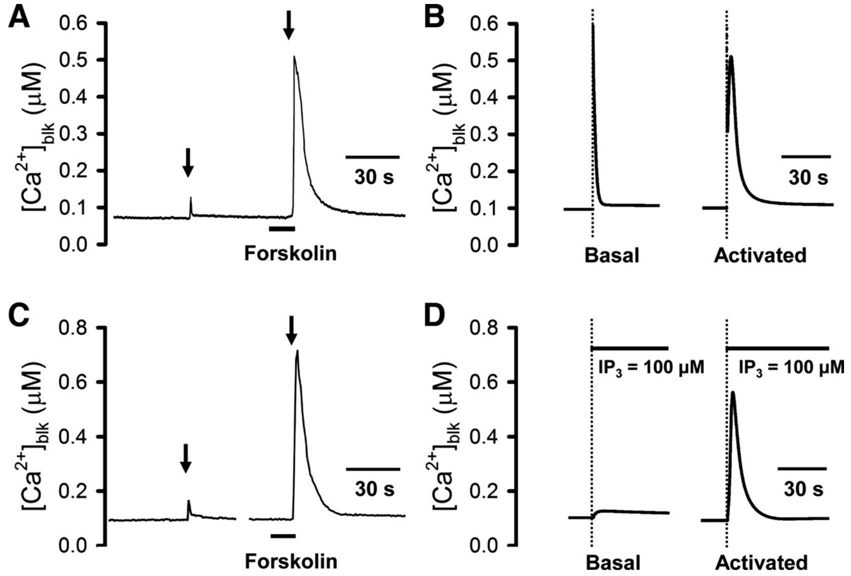

Fig. 3. Simulation of Ca^{2+} transients triggered by an abrupt increase of [Ca^{2+}] and [IP$_3$] in β-cells. *A*: experimental data (25) in which a mouse β-cell was loaded with fura-2-AM and caged Ca^{2+} (NP-EGTA-AM) so that Ca^{2+} could be uncaged by UV flash photolysis of NP-EGTA. The duration of the UV flash was 600 μs. Uncaging of Ca^{2+} was performed under control conditions in the absence of forskolin (*left arrow*) or under test conditions in which forskolin (2 μM) was applied directly to the cell (*right arrow*). Due to the relatively slow fura-2 sampling rate (0.5 Hz), the amplitude of the Ca^{2+} transient measured under control conditions is an underestimate of the true amplitude measured immediately after the 600 μs UV stimulus. *B*: simulation of the Ca^{2+} transients induced by the uncaging of Ca^{2+}, for comparison with *A*. To initiate Ca^{2+} transients, UV flash photolysis of NP-EGTA was simulated mathematically by injecting Ca^{2+} (dotted lines) at a rate of 40 fmol/s for 1 ms under control conditions (Basal) or under test conditions that mimic the action of forskolin (Activated). [IP$_3$] was held at 2 μM throughout the simulation experiments. *C*: experimental data (25) in which Ca^{2+} transients were measured in a mouse β-cell after UV flash photolysis of caged IP$_3$ (ci-IP$_3$/PM) for control conditions in the absence of forskolin (*left arrow*) or test conditions in the presence of 2 μM forskolin (*right arrow*). *D*: simulation of the Ca^{2+} transients induced by the uncaging of IP$_3$ for comparison with *C*. To initiate Ca^{2+} transients under control conditions in the absence of forskolin (Basal) or under test conditions in the presence of forskolin (Activated), the [IP$_3$] (black bars) was increased from 2 to 100 μM in a step-wise manner (dotted lines indicate start of stimulus). For simulations in *B* and *D*, P_{IP3R} = 13.65 fl/ms and P_{SERCA} = 0.069 amol/ms were set for Basal conditions, whereas P_{IP3R} = 174.72 fl/ms and P_{SERCA} = 0.23 amol/ms were set for Activated conditions, respectively.

coefficient $n_H = 2$. P_{SERCA} the maximum molar flux of SERCA with a unit of amol/ms.

$$J_{SERCA} = P_{SERCA} \cdot \frac{1}{1+\left(\frac{K_d}{[Ca^{2+}]_{blk}}\right)^{n_H}} \tag{11}$$

The rate of changes in $[Ca^{2+}]_{blk}$, $[Ca^{2+}]_{nrs}$, and $[Ca^{2+}]_{ER}$ were described by *Eqs. 12*, *13*, and 14, respectively, where vol$_x$ is the volume of the corresponding Ca^{2+} compartment *x*. In contrast, f_i and f_{ER} (Table 2) are fractions of free Ca^{2+} in cytosol and in ER, respectively, considering buffering capacity of Ca^{2+} in each compartment (5). J_{flash} in *Eqs. 12* and *13* indicates the flux of Ca^{2+} by Ca^{2+} injection applied in Figs. 3 and 4.

$$\frac{d[Ca^{2+}]_{blk}}{dt} = \frac{f_i}{vol_{blk}} \cdot (J_{nrsblk} - J_{SERCA} + J_{mleak} + J_{flash}) \tag{12}$$

$$\frac{d[Ca^{2+}]_{nrs}}{dt} = \frac{f_i}{vol_{nrs}} \cdot \left(J_{IP3R} - J_{ERleak} + J_{nrsblk} + J_{flash} \cdot \frac{vol_{nrs}}{vol_{blk}}\right) \tag{13}$$

$$\frac{d[Ca^{2+}]_{ER}}{dt} = \frac{f_{ER}}{vol_{ER}} \cdot (J_{SERCA} - J_{IP3R} + J_{ERleak}) \tag{14}$$

In these mathematical analyses, J_{mleak} was set to zero for simplicity. Thus intracellular total Ca^{2+} content ($Ca^{2+}{}_{tot}$) was kept constant. This approach revealed mechanisms of Ca^{2+} mobilization that are intrinsic to ER function and that are determined by activities of the IP$_3$R and SERCA. Redundancy in calculating Ca^{2+} concentrations at all subcellular compartments was avoided by omitting *Eq. 14* but applying the Ca^{2+} conservation below (*Eq. 15*).

$$[Ca^{2+}]_{ER} = \frac{f_{ER}}{vol_{ER}} \cdot \left(Ca^{2+}_{tot} - \frac{vol_{blk}}{f_i}[Ca^{2+}]_{blk} - \frac{vol_{nrs}}{f_i}[Ca^{2+}]_{nrs}\right) \tag{15}$$

P_{IP3R} and P_{SERCA} (Table 2) were determined on the basis of passive Ca^{2+} leak and J_{SERCA}, respectively, for the full β-cell model describing the nonbursting period (5). V_{nrs}, as well as P_{ERleak}, P_{nrsblk}, and P_{mleak}, were estimated by reproducing the resting $[Ca^{2+}]_{blk}$, $[Ca^{2+}]_{ER}$, and the time course of the decay of released Ca^{2+} under control conditions (see Fig. 3*A*). Parameters for V_{nrs} and P_{nrsblk}, however, are not unique in satisfying the resting cellular conditions. Decreasing V_{nrs} in concert with increasing P_{nrsblk}, for example, would provide the analogous result. P_{IP3R} as well as P_{SERCA} in the presence of forskolin, a cAMP-elevating agent, were also estimated by reproducing the Ca^{2+}-induced Ca^{2+} transient (in Fig. 3*A*).

Bifurcation analysis. Bifurcation analysis is a mathematical approach to investigate changes in model behavior (whether it converges, diverges, or oscillates) initiated by continuous alteration in the value of a given model parameter. More specifically, this analysis examines bifurcations of stationary and periodic steady-state solutions of the model; equilibrium points (EPs) and limit cycles (LCs), respectively. For the model described here, each of the key parameters ($Ca^{2+}{}_{tot}$, P_{IP3R}, P_{SERCA}, α_{CaA}, and α_{CaI}) was systematically varied with the objective to determine how the $[Ca^{2+}]_{nrs}$ transitions from a stable stationary behavior (at the EP) to a spontaneously generating oscillatory pattern (within a LC). For this analysis, the positions and stabilities of the steady states were automatically obtained by directly finding roots of the model equation system using XPPAUT, a computational tool for bifurcation analysis.

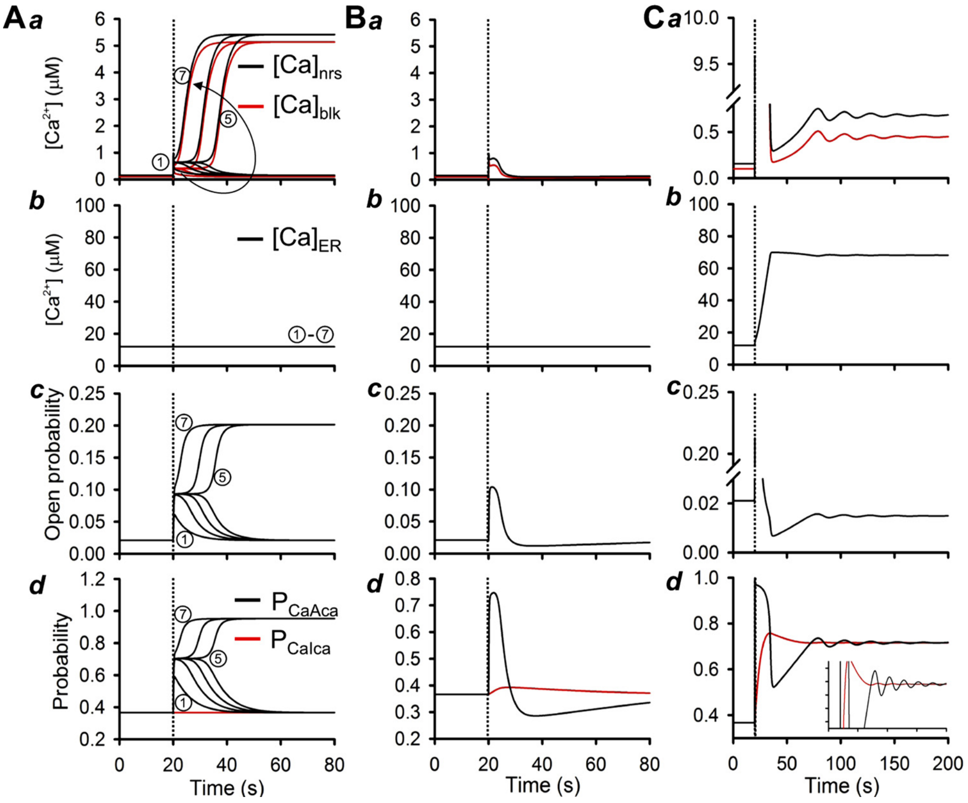

Fig. 4. Ca^{2+}-dependent positive and negative feedback regulation of the IP$_3$R during dynamic Ca^{2+} mobilization. *A–C*: [Ca^{2+}]$_{nrs}$ and [Ca^{2+}]$_{blk}$ (*a*) were plotted along with [Ca^{2+}]$_{ER}$ (*b*) and P_o (*c*), including P_{CaAca} and P_{CaIca} of the IP$_3$R (*d*), before and after Ca^{2+} injections. As in the simulation study of Fig. 3 (*B*), Ca^{2+} was injected at a rate of 40 fmol/s for 1 ms (IP$_3$ = 2 μM). *A*, Effects of gradual increases in the intensities of Ca^{2+} injection, from 40 to 60 fmol/s (①: 40; ②: 54; ③: 54.45; ④: 54.50; ⑤: 54.52; ⑥: 54.7; and ⑦: 60 fmol/s as indicated by an arrow), while P_{CaIca} and [Ca^{2+}]$_{ER}$ were both fixed at the corresponding resting levels. Responses to the Ca^{2+} injection at 60 fmol/s (⑦ in *A*) were compared with those simulated without fixing P_{CaIca} at the resting level (*B*). *C*: responses to Ca^{2+} injection at 650 fmol/s. Changes in P_{CaIca} and [Ca^{2+}]$_{ER}$ were both calculated for this simulations. Trace in *Cd* between probabilities of 0.65–0.75 is expanded at *bottom*.

Instantaneous equilibrium analysis. To examine mechanisms that contribute to dynamic IP$_3$R-mediated Ca^{2+} oscillations, we applied instantaneous equilibrium (IE) analysis (39) to a minimal β-cell model. IE analysis is a simulation-based analysis, and it can be used to quantify the contributions of all differential variables (i.e., P_{CaAca}, P_{CaIca}, and [Ca^{2+}]$_{blk}$) to changes in [Ca^{2+}]$_{nrs}$ in the minimal cell model (Fig. 6). This is obtained by calculating an IE point of [Ca^{2+}]$_{nrs}$ (^{IE}[Ca^{2+}]$_{nrs}$) at each moment. ^{IE}[Ca^{2+}]$_{nrs}$ is the [Ca^{2+}]$_{nrs}$ when the rate of change in [Ca^{2+}]$_{nrs}$ (J_{IP3R} + J_{ERleak} − J_{nrsblk}) described by *Eq. 13* equals 0 for a condition where every variable but [Ca^{2+}]$_{nrs}$ is fixed at a every time point. ^{IE}[Ca^{2+}]$_{nrs}$ was determined by *Eq. 16* (see Ref. 39 for the derivation).

$$^{IE}\left[Ca^{2+}\right]_{nrs} = \frac{P_{IP3R}\cdot P_o\cdot\left[Ca^{2+}\right]_{ER} + P_{ERleak}\cdot\left[Ca^{2+}\right]_{ER} + P_{nrsblk}\cdot\left[Ca^{2+}\right]_{blk}}{P_{IP3R}\cdot P_o + P_{ERleak} + P_{nrsblk}} \tag{16}$$

Eq. 13 can be deformed into the following equation (J_{flash} was not included for oscillation studies).

$$\frac{d\left[Ca^{2+}\right]_{nrs}}{dt} = \frac{f_i}{vol_{nrs}}\left(P_{IP3R}\cdot P_o + P_{ERleak} + P_{nrsblk}\right)\left({}^{IE}\left[Ca^{2+}\right]_{nrs} - \left[Ca^{2+}\right]_{nrs}\right) \tag{17}$$

Since ^{IE}[Ca^{2+}]$_{nrs}$ is a momentary equilibrium concentration of [Ca^{2+}]$_{nrs}$, ^{IE}[Ca^{2+}]$_{nrs}$ always moves in advance of [Ca^{2+}]$_{nrs}$, and thus its time derivative, d^{IE}[Ca^{2+}]$_{nrs}$/d*t* drives the change in [Ca^{2+}]$_{nrs}$. The contribution (*c*) of a variable of interest, *i*, to the rate of change in ^{IE}[Ca^{2+}]$_{nrs}$ can be calculated by multiplying the partial derivative of ^{IE}[Ca^{2+}]$_{nrs}$ with respect to the variable of interest, *i*, and the rate of change in the parameter (*Eq. 18*). Summation of the contributions, *c*, from every variable in the cellular model made up the d^{IE}[Ca^{2+}]$_{nrs}$/d*t*. Consequently, *c* represents an *i*-component of d^{IE}[Ca^{2+}]$_{nrs}$/d*t*, or a quantified contribution of the variable of interest *i* to changes in [Ca^{2+}]$_{nrs}$. See Shimayoshi et al. (39) for additional details.

$$c = \frac{\partial^{IE}\left[Ca^{2+}\right]_{nrs}}{\partial_i}\cdot\frac{di}{dt} \tag{18}$$

RESULTS

Simulation studies of Ca^{2+}- and IP$_3$-induced ER Ca^{2+} release in mouse β-cells. Kang et al. (25) reported that for mouse β-cells loaded with a membrane permeable caged Ca^{2+} (NP-EGTA-AM), it was possible to use short-duration, low-intensity UV flash photolysis to uncage Ca^{2+} to examine how Ca^{2+} and cAMP functionally interact to facilitate CICR originating from IP$_3$R-regulated ER Ca^{2+} stores. Under control conditions in which β-cells were not exposed to a cAMP-elevating agent, the uncaging of Ca^{2+} generated a small increase of [Ca^{2+}]$_i$ (Fig. 3*A*, *left arrow*) that was not considered to result from ER Ca^{2+} mobilization. However, for β-cells treated with the cAMP-elevating agent forskolin, ER Ca^{2+} mobilization resulting from CICR was observed (Fig. 3*A*, *right arrow*), as defined by Kang et al. (25). With this available information in hand, we sought to model the underlying processes of ER Ca^{2+} mobilization.

For the mathematical simulation studies reported here, UV flash photolysis-induced uncaging of Ca^{2+} in the absence of forskolin was simulated as a step-wise intracellular "injection" of Ca^{2+} at a rate of 40 fmol/s into the bulk (blk) cytosolic space for 1 ms while also injecting Ca^{2+} near the release site (nrs) at which IP$_3$R Ca^{2+} release events occur (*left trace* of Fig. 3*B*, injection time indicated by dotted lines; see *Eq. 12*). For both injection procedures, the increase of [Ca^{2+}]$_{blk}$ after Ca^{2+}

injection was precisely matched to the increase of [Ca^{2+}]$_{nrs}$ after Ca^{2+} injection (*see Eq. 13*). For this simulation performed in the absence of forskolin (Fig. 3*B*, *left trace*), the [Ca^{2+}]$_{blk}$ quickly rose to ~0.6 μM during injection of Ca^{2+}. However, the response immediately decayed after the offset of injection without generating CICR, as was also the case for the experiment reported by Kang et al. (Fig. 3*A*, *left arrow*). To obtain these findings, the [IP$_3$] was fixed at the basal concentration of ~2 μM, and P_{IP3R} and P_{SERCA} were also set at basal activity levels of 13.65 fl/ms and 0.069 amol/ms, respectively (see Table 2).

To model the sensitizing action of forskolin at the IP$_3$R, the value for P_{IP3R} was increased, a manipulation that simulates PKA-mediated phosphorylation of the IP$_3$R (41). Simultaneously, P_{SERCA} was also increased to simulate the higher turnover rate of SERCA that occurs when levels of cAMP are increased (46). CICR was successfully initiated ~400 ms after Ca^{2+} injection when P_{IP3R} and P_{SERCA} were increased to 174.72 fl/ms and 0.23 amol/ms, respectively (Fig. 3*B*, *right trace*). Properties describing the amplitude and time course of this simulated CICR (peak = 0.5 μM, time-to-peak = 2.2 s, and duration at the 50% amplitude cut-off = 5.6 s) were comparable to that of the Ca^{2+} transient measured by Kang et al. (Fig. 3*A*, *right arrow*) for mouse β-cells treated with forskolin (peak = 0.422 ± 0.063 μM, time-to-peak = 2.98 ± 1.69 s, and duration at the 50% amplitude cut-off = 7.6 ± 1.9 s). P_{IP3R} and P_{SERCA} values of 174.72 fl/ms and 0.23 amol/ms, respectively, provided the best match for simulated and experimental CICR when comparing these properties of Ca^{2+} transient amplitude and duration.

Kang et al. (25) also reported that a membrane permeable caged IP$_3$ (ci-IP3/PM) could be used in combination with UV flash photolysis to evaluate how forskolin facilitates IP$_3$R-mediated Ca^{2+} mobilization in β-cells. In the absence of forskolin, the uncaging of IP$_3$ produced a small increase of Ca^{2+} (Fig. 3*C*, *left arrow*), whereas a Ca^{2+} transient with properties similar to CICR was initiated in β-cells treated with forskolin (Fig. 3*C*, *right arrow*). For these β-cells treated with forskolin, experimental properties describing the amplitude and time course of the Ca^{2+} transient triggered by the uncaging of IP$_3$ (peak = 0.528 ± 0.096 μM, time-to-peak = 4 ms, and duration at the 50% amplitude cut off = 8.8 ms) matched closely those measured under conditions in which the Ca^{2+} transient was instead triggered by the uncaging of Ca^{2+} (see above).

To simulate experimental findings obtained with caged IP$_3$, the [IP$_3$] was increased in a step-wise manner from an initial value of 2 μM to final value of 100 μM. This final value was then maintained for the whole time course of the simulation (Fig. 3*D*, black horizontal bars). For the sake of simplicity, the rate of degradation of IP$_3$ was not considered. Continuous elevation of [IP$_3$] stimulated only a small increase of [Ca^{2+}]$_i$ when values of P_{IP3R} and P_{SERCA} were set at "basal" levels (Fig. 3*D*, *left trace*) analogous to experimental findings obtained in the absence of forskolin (Fig. 3*C*, *left arrow*). These basal levels for P_{IP3R} and P_{SERCA} corresponded to 13.65 fl/ms and 0.069 amol/ms, respectively.

To model findings obtained for β-cells treated with forskolin, the values of P_{IP3R} and P_{SERCA} were increased to "activated" levels that corresponded to 174.72 fl/ms and 0.23 amol/ms, respectively. Under these conditions, the Ca^{2+} transient generated by a simulated step-wise increase of [IP$_3$] (Fig. 3*D*, *right trace*) matched closely that of the Ca^{2+} transient induced by uncaging of IP$_3$ in β-cells treated with forskolin (Fig. 3*C*, *right arrow*). Properties describing the amplitude and time course of the IP$_3$-induced Ca^{2+} response under activated conditions in this simulation yielded the following values: peak = 0.56 μM, time-to-peak = 3.0 s, and duration at the 50% amplitude cut off = 5.9 s.

When considering these findings obtained in simulation studies that mimic the uncaging of Ca^{2+} (Fig. 3*B*) or the uncaging of IP$_3$ (Fig. 3*D*), and when also considering data in Fig. 1 concerning IP$_3$R open channel probability, it may be concluded that the present model of IP$_3$R-mediated Ca^{2+} mobilization faithfully reproduced experimental findings obtained using mouse β-cells (25). Furthermore, these simulation studies indicated that the β-cell IP$_3$R acts as a molecular coincidence detector in which its gating function is regulated not only by IP$_3$ and Ca^{2+} but also by cAMP signaling pathways.

Dynamic mechanisms for initiation and termination of Ca^{2+} transients. During the initiation of CICR, a fraction of the ER Ca^{2+} that is released might bind to the CaA site on the IP$_3$R, and progressively create positive feedback activation of the IP$_3$R. On the other hand, termination of CICR might result either from simultaneous binding of Ca^{2+} to the receptor's CaI site or from depletion of ER Ca^{2+} content. To reveal the dynamic mechanisms for initiation and termination of CICR, simulation experiments were performed by dissecting these competitive interactions among P_{CaAca}, P_{CaIca}, and [Ca^{2+}]$_{ER}$. First, to investigate how the positive feedback involving Ca^{2+}-dependent activation of the IP$_3$R may be triggered, [Ca^{2+}]$_{nrs}$ and [Ca^{2+}]$_{blk}$ were monitored after injection of Ca^{2+} with increasing flux (as indicated by an arrow) from 40 to ~60 fmol/s for 1 ms (Fig. 4*Aa*). For this simulation, P_{CaIca} and [Ca^{2+}]$_{ER}$ were both fixed at the resting conditions (see Fig. 4, *Ab* and *Ad*), and J_{mleak} was excluded to reveal mechanisms of Ca^{2+} mobilization that are intrinsic to ER function.

When Ca^{2+} injection was stimulated with a rate of 40 fmol/s, J_{efflux} (J_{IP3R} + J_{ERleak}) and J_{SERCA} increased due to Ca^{2+}-dependent activation of IP$_3$R and SERCA pump, respectively (data now shown). J_{efflux}, however, did not exceed J_{SERCA} and thus [Ca^{2+}]$_{nrs}$ and [Ca^{2+}]$_{blk}$ started to gradually decay to the resting levels (Fig. 4*Aa*, ①). When the Ca^{2+} injection became strong enough to outrun the threshold (see Fig. 4*Aa*, ⑤; 54.52 fmol/s), J_{efflux} was elevated over J_{SERCA} (data now shown), further increasing [Ca^{2+}]$_{nrs}$ and [Ca^{2+}]$_{blk}$ to a saturating level (Fig. 4*Aa*, ⑤–⑦) where J_{efflux} balanced with J_{SERCA}. Involvement of a positive feedback loop for activation of the IP$_3$R was well revealed by increasing P_{CaAca} (Fig. 4*Ad*) along with P_o (Fig. 4*Ac*) for the rising phase of [Ca^{2+}]$_{nrs}$. Note that the rate of the initial rising phase became faster with a stronger Ca^{2+} stimulus, whereas common sigmoidal time courses for self-regenerating responses were observed once positive feedback was triggered.

Next, we investigated whether binding of Ca^{2+} to the receptor's CaI site contributes to the termination of Ca^{2+} transients. To this end, the change in P_{CaIca} was calculated along with P_{CaAca}, whereas [Ca^{2+}]$_{ER}$ remained fixed at the resting conditions for this simulation (Fig. 4, *Ba-Bd*). When Ca^{2+} injection of 60 fmol/s was applied, similarly to Fig. 4*Aa*⑦, P_{CaIca} was slowly increased as [Ca^{2+}]$_{nrs}$ was elevated, compared with the rate of change in P_{CaAca}. This slow change in P_{CaIca} caused a disturbance of the self-regenerating positive feedback activation of IP$_3$R (see Fig. 4, *Bc* and *Bd*) and an acceleration of the decay of the Ca^{2+} response (Fig. 4*Ba*). Failure to generate the full positive feedback responses was because J_{SERCA} was elevated over J_{efflux} due to a gradual increase in P_{CaIca} (data not shown). Although [Ca^{2+}]$_{\mathrm{ER}}$ was constant (Fig. 4*Bb*), the rate of the decay in the Ca^{2+} response was quite similar to that of Ca^{2+} transient in Fig. 3. Thus the slow rate of change in P_{CaIca} was predominantly determined by the rate of decay in the Ca^{2+} response.

When the change in [Ca^{2+}]$_{\mathrm{ER}}$ was also calculated, a strong Ca^{2+} injection (650 fmol/s) caused a remarkable increase in [Ca^{2+}]$_{\mathrm{ER}}$ (Fig. 4*Cb*) and Ca$^{2+}_{\mathrm{tot}}$ (data not shown) within the minimal cell model from a control level of 11.92 μM and 141.18 amol to 68.15 μM and 797.83 amol, respectively. It also induced a notable increase in [Ca^{2+}]$_{\mathrm{blk}}$ and [Ca^{2+}]$_{\mathrm{nrs}}$ (Fig. 4*Ca*), whereas these Ca^{2+} levels quickly decayed as P_{o} of the IP$_3$R was reduced (Fig. 4*Cc*) along with a large increase in P_{CaIca} (Fig. 4*Cd*). Interestingly, these decreases in intracellular Ca^{2+} responses were followed with a marked sign of Ca^{2+} oscillations.

Taken together, initiation of CICR occurs when Ca^{2+} or IP$_3$ stimulation activates the IP$_3$R enough to elevate J_{efflux} (J_{IP3R} + J_{ERleak}) over J_{SERCA} (data not shown). Sequential rising and falling phases, followed by an autonomous termination of CICR in an intact system, are predominantly determined by the balance between the time courses of Ca^{2+}-dependent activation and inhibition of the IP$_3$R. This sequential change in Ca^{2+}-dependent activation and inhibition of the IP$_3$R (Fig. 4*Cd*) may also be responsible for the oscillatory behavior of [Ca^{2+}]$_{\mathrm{nrs}}$. The mechanisms underlying the behavioral changes in [Ca^{2+}]$_{\mathrm{nrs}}$ were further investigated in the following bifurcation analysis.

Bifurcation analysis reveals behavioral characteristics of the model. The simulations described above demonstrated that the IP$_3$R exhibited fundamental properties of sequential positive and negative feedback regulation due to fast activation and slow inhibition of the channel by Ca^{2+}. Such findings strongly suggest that the herein described IP$_3$R model for CICR has the potential to also predict how oscillations of [Ca^{2+}]$_{\mathrm{i}}$ are generated. Thus bifurcation analysis was performed to test this hypothesis, while also considering intracellular conditions within the minimal cell model that allow oscillations of [Ca^{2+}]$_{\mathrm{i}}$ to take place. Behavioral characteristics of [Ca^{2+}]$_{\mathrm{nrs}}$ were investigated by examining steady-state solutions; i.e., EPs and LCs of the model as a function of key model parameters, Ca$^{2+}_{\mathrm{tot}}$, P_{IP3R}, P_{SERCA}, α_{CaA}, and α_{CaI}. Figure 5*A* shows mode changes in [Ca^{2+}]$_{\mathrm{nrs}}$ induced by increasing Ca$^{2+}_{\mathrm{tot}}$, from 0 to ~3,000 amol, under simulated conditions with a constant [IP$_3$] (2 μM). When Ca$^{2+}_{\mathrm{tot}}$ was set at a resting cellular level (141.2 amol, *dotted line a*), only a stable EP appeared. This indicated that [Ca^{2+}]$_{\mathrm{nrs}}$ was stabilized on the EP at 0.156 μM (corresponding to the resting [Ca^{2+}]$_{\mathrm{nrs}}$, *right a*) even with the activated IP$_3$R and SERCA pump.

On the other hand, Fig. 5*A* exhibited a stable LC as Ca$^{2+}_{\mathrm{tot}}$ was raised above the first bifurcation point of 832.9 amol, suggesting spontaneous oscillations of [Ca^{2+}]$_{\mathrm{i}}$. [Ca^{2+}]$_{\mathrm{nrs}}$ oscillations occurring within the range of 0.51~1.14 μM (indicated by the stable LC at the *solid line b*) were predicted when Ca$^{2+}_{\mathrm{tot}}$ reached 920.3 amol, an estimated total intracellular Ca^{2+} content that existed during the bursting period in a full-cell model simulation (5). The upper and lower range of the LC (0.51~1.14 μM) matched well to that of [Ca^{2+}]$_{\mathrm{nrs}}$ oscillations, *right b*. When Ca$^{2+}_{\mathrm{tot}}$ increased above 2,522.6 amol, LCs disappeared, indicating termination of the oscillations, and stabilization of [Ca^{2+}]$_{\mathrm{nrs}}$ at the corresponding stable EP. Ca$^{2+}_{\mathrm{tot}}$ was set at 920.3 amol as a reference for the following bifurcation analysis.

Next, we considered how IP$_3$R and SERCA activity levels participate in the generation of Ca^{2+} oscillations. As Fig. 5*B* indicates, an increase in P_{IP3R} from a basal (13.65 fl/ms, at the dotted line) to an activated level (174.72 fl/ms, at the solid line) converted [Ca^{2+}]$_{\mathrm{nrs}}$ from a stable to an oscillatory pattern. Thus appropriate increases in P_{IP3R} to levels within the range that produced stable limit cycles may, indeed, cause sustained oscillation in [Ca^{2+}]$_{\mathrm{nrs}}$. When [IP$_3$] was elevated, oscillations were predicted to occur at a lower range for P_{IP3R} (data not shown). In a similar manner, a mode change in the behavioral pattern of [Ca^{2+}]$_{\mathrm{nrs}}$ was achieved by increasing P_{SERCA} from the resting (0.07 amol/ms, at the dotted line) to enhanced activity level (0.23 amol/ms, at the solid line).

Critical rate constants of Ca^{2+}-dependent activation and inhibition of the IP$_3$R for the generation of [Ca^{2+}]$_{\mathrm{nrs}}$ oscillations were also examined. As for Fig. 5, *A*–*C*, EPs and LCs of [Ca^{2+}]$_{\mathrm{nrs}}$ were obtained as a function of varying α_{CaA} (Fig. 5*D*) and α_{CaI} (Fig. 5*E*). Accompanying β_{CaA} and β_{CaI}, respectively, were systematically modified so that corresponding dissociation constants (K_{dCaA} and K_{dCAI}) remained constant throughout the analyses. Since α_{CaA}, estimated by the simulation study in Fig. 3 (6 mM/ms, at the solid line in Fig. 5*D*), was remarkably faster than α_{CaI} (1.5 E-2 mM^{-1}·ms^{-1}, solid line in Fig. 5*E*), a slight change in α_{CaA} did not cause a significant effect on the oscillatory pattern for [Ca^{2+}]$_{\mathrm{nrs}}$, unless it was below the bifurcation point (α_{CaA} = 0.69 mM^{-1}·ms^{-1}). A modest rise in α_{CaI}, on the other hand, reduced the amplitude of [Ca^{2+}]$_{\mathrm{nrs}}$ oscillations and eventually stabilized [Ca^{2+}]$_{\mathrm{nrs}}$ at corresponding stable EPs if α_{CaI} became faster than 0.69 mM^{-1}·ms^{-1}, where a bifurcation occurred. Thus bifurcation analysis revealed the key parameters (Ca$_{\mathrm{tot}}$, P_{IP3R}, P_{SERCA}, α_{CaA}, and α_{CaI}), which allow for IP$_3$R-mediated oscillatory Ca^{2+} mobilization.

IE analysis of the IP$_3$R-mediated Ca^{2+} oscillations in pancreatic β-cells. Although the bifurcation analysis successfully described the key parameters summarized above, the dynamic mechanisms describing how Ca^{2+} oscillations are generated at given parameter sets remained elusive. To systematically analyze the quantitative mechanisms underlying IP$_3$R-mediated Ca^{2+} oscillations, IE analysis of [Ca^{2+}]$_{\mathrm{nrs}}$ was performed. The equilibrium [Ca^{2+}]$_{\mathrm{nrs}}$ at each time point ($^{\mathrm{IE}}$[Ca^{2+}]$_{\mathrm{nrs}}$) was plotted along with [Ca^{2+}]$_{\mathrm{nrs}}$ in Fig. 6*A*. Although $^{\mathrm{IE}}$[Ca^{2+}]$_{\mathrm{nrs}}$ always moved in advance of [Ca^{2+}]$_{\mathrm{nrs}}$, [Ca^{2+}]$_{\mathrm{nrs}}$ apparently overlapped with $^{\mathrm{IE}}$[Ca^{2+}]$_{\mathrm{nrs}}$, suggesting that the oscillation occurred nearly at the instantaneous equilibrium. Corresponding time courses of changes in P_{CaAca} and P_{CaIca} during [Ca^{2+}]$_{\mathrm{nrs}}$ oscillations in Fig. 6*A* are shown in Fig. 6*B*. Note that for these simulations, the cyclic increases (or decreases) in P_{CaIca} were delayed from P_{CaAca} by approximately one-half cycle, exhibiting antiphasic changes in the activation and inactivation parameters.

Contributions of P_{CaAca}, P_{CaIca}, and [Ca^{2+}]$_{\mathrm{blk}}$ toward the rate of change in $^{\mathrm{IE}}$[Ca^{2+}]$_{\mathrm{nrs}}$ (d$^{\mathrm{IE}}$[Ca^{2+}]$_{\mathrm{nrs}}$/d*t*) are indicated in

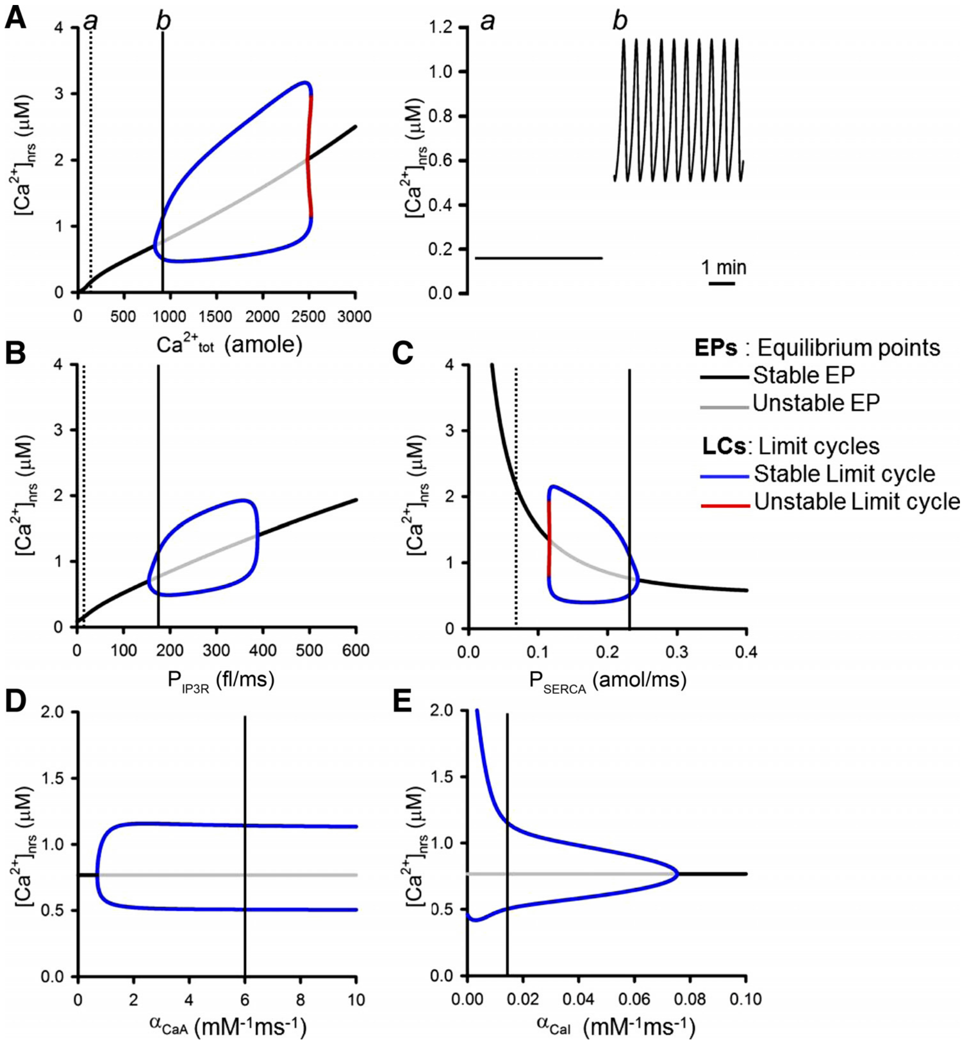

Fig. 5. Bifurcation analysis demonstrated how model parameters alter oscillatory behavior at [Ca^{2+}]$_{nrs}$. Steady-state solutions, equilibrium points (EPs), and limit cycles (LCs) of [Ca^{2+}]$_{nrs}$ are plotted as functions of various model parameters; Ca$^{2+}_{tot}$ (*A*), P_{IP3R} (*B*), P_{SERCA} (*C*), α_{CaA} (*D*), and α_{CaI} (*E*). A LC is represented with two lines: the minimum and maximum values in the oscillation. Parameters in *A* at the dotted lines (*a*) are for Ca$^{2+}_{tot}$ expected during the cellular quiescent period (141.2 amol). Ca$^{2+}_{tot}$ at the solid line (*b*), on the other hand, represents estimated total Ca^{2+} content during glucose-induced continuous bursting in β-cells (920.3 amol). Time-dependent simulation of [Ca^{2+}]$_{nrs}$ using the parameters *a* and *b* are shown at *right*. P_{IP3R} and P_{SERCA} in *B* and *C* at dotted lines represent the basal activity levels for the IP$_3$R and SERCA (P_{IP3R} = 13.65 fl/ms, P_{SERCA} = 0.07 amol/ms), respectively, whereas those at the solid lines exhibit the activated levels (P_{IP3R} = 174.72 fl/ms, P_{SERCA} = 0.23 amol/ms), presumably, during agonist-induced elevation of [cAMP]. α_{CaA} and α_{CaI}, at the solid lines in *D* and *E* (6 mM^{-1}·ms^{-1} and 1.5 E-2 mM^{-1}·ms^{-1}), respectively, are rate constants determined by reproducing Ca^{2+}-induced Ca^{2+} release in Fig. 3.

Fig. 6*C* in a unit of uM/s (see *Eq. 18*) to elucidate the variable component primarily driving the ^{IE}[Ca^{2+}]$_{nrs}$ oscillations. For this analysis, at the inflection point of ^{IE}[Ca^{2+}]$_{nrs}$, from descending to ascending phases, where the d^{IE}[Ca^{2+}]$_{nrs}$/d*t* switched from negative to positive (~7.8 s in Fig. 6*C*), P_{CaIca} was the only variable that provided a positive contribution, specifically, from ~2 s before the inflection point (see the expanded trace in Fig. 6*D*). Thus P_{CaIca} was the key factor to drive the increase of ^{IE}[Ca^{2+}]$_{nrs}$. For these simulations, reducing Ca^{2+}-dependent inhibition of the IP$_3$R during the decay phase of [Ca^{2+}]$_{nrs}$ (see Fig. 6*B*) conferred an increased P_o for the channel and subsequently drove the increase of [Ca^{2+}]$_{nrs}$. Rate of change in P_{CaIca} thus provided a significant impact on the rate of change in [Ca^{2+}]$_{nrs}$ and therefore the frequency of [Ca^{2+}]$_{nrs}$ oscillations. On the other hand, [Ca^{2+}]$_{blk}$ and P_{CaAca} provided larger positive contributions than P_{CaIca} to d^{IE}[Ca^{2+}]$_{nrs}$/d*t* but only after the inflection point of ^{IE}[Ca^{2+}]$_{nrs}$. Once [Ca^{2+}]$_{nrs}$ began to increase, [Ca^{2+}]$_{blk}$ also increased, accelerating the rise in d^{IE}[Ca^{2+}]$_{nrs}$/d*t* by reducing Ca^{2+} efflux from nrs site (J_{nrsblk}, see *Eq. 10*).

Note that for these simulations, SERCA negatively contributed to the rate of rise in [Ca^{2+}]$_{blk}$ as the concentration of Ca^{2+} increased. However, [Ca^{2+}]$_{blk}$ continued to rise due to J_{efflux} exceeding J_{SERCA} (data not shown). The positive contribution of P_{CaAca} to the rate of rise in [Ca^{2+}]$_{blk}$ reflected positive feedback regulation involving Ca^{2+-}-dependent stimulation of the channel, actively increasing d^{IE}[Ca^{2+}]$_{nrs}$/d*t*. For this analysis, a contribution of $P_{IP3Hip3}$ to d^{IE}[Ca^{2+}]$_{nrs}$/d*t* is not shown in Fig. 6, *C*–*E*, since it was negligibly small. Finally, note that the inflection point from ascending to descending phases of ^{IE}[Ca^{2+}]$_{nrs}$ (Fig. 6*A*) was explained by a similar but opposite mechanism to the one described above. The positive rate of change in ^{IE}[Ca^{2+}]$_{nrs}$ that switched to negative (~28.3 s in Fig. 6*C*, expanded in the Fig. 6*E*) was a result of increased P_{CaIca} (see Fig. 6*B*). Decreasing [Ca^{2+}]$_{blk}$ and P_{CaAca} amplified the decay in ^{IE}[Ca^{2+}]$_{nrs}$ after [Ca^{2+}]$_{nrs}$ started to decline. This analysis revealed that the slow rate of change in P_{CaIca} drove and paced Ca^{2+} oscillations.

DISCUSSION

Modeling IP$_3$R function under the control of GLP-1 in pancreatic β-cells. In the theoretical analysis presented here, cellular mechanisms of IP$_3$R regulation were investigated to better understand how GLP-1 mobilizes Ca^{2+}, while also stimulating global oscillations of [Ca^{2+}]$_i$. Our analysis took advantage of a new dynamic IP$_3$R1 model that allowed simulation studies to be performed so that novel aspects of IP$_3$R

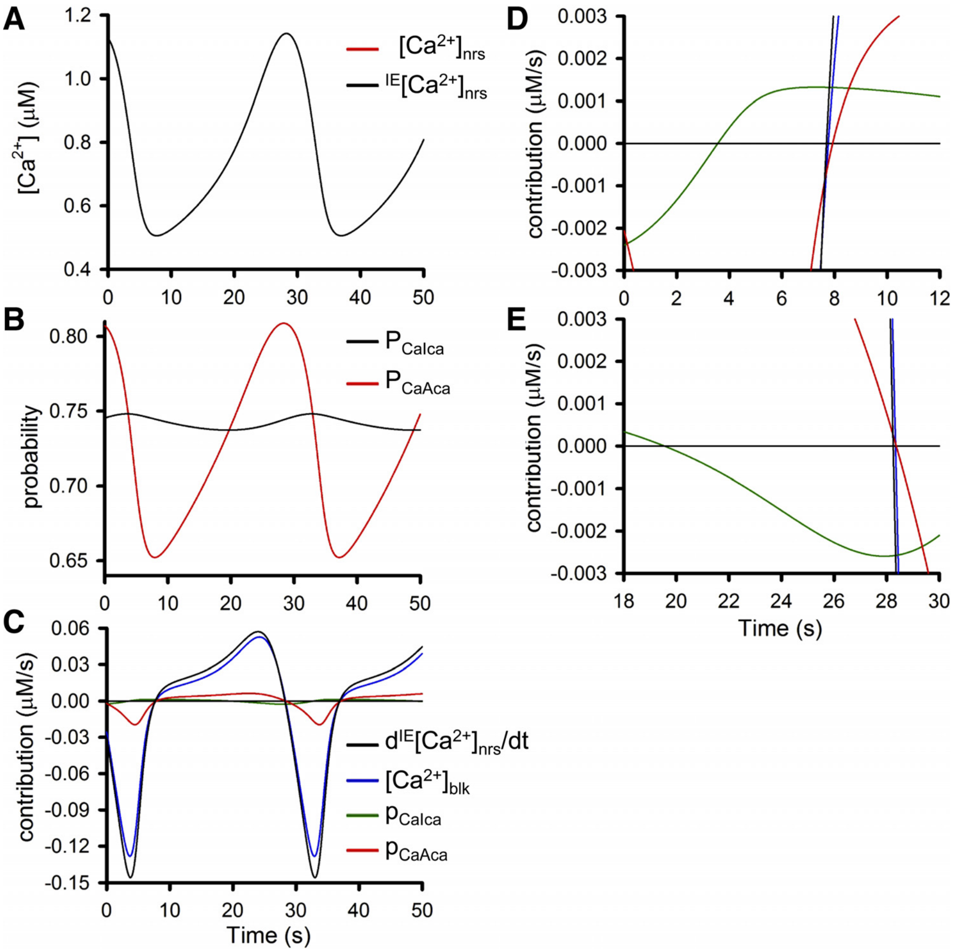

Fig. 6. Instantaneous equilibrium (IE) analysis for the quantitative mechanisms underlying IP$_3$R-mediated Ca^{2+} oscillations in β-cells. The time course in 1 full cycle of the [Ca^{2+}]$_{nrs}$ oscillation was plotted with ^{IE}[Ca^{2+}]$_{nrs}$ in *A*, and the corresponding rate of change in ^{IE}[Ca^{2+}]$_{nrs}$ along with the contributions of variables; [Ca^{2+}]$_{blk}$, P_{CaIca}, and P_{CaAca} toward ^{IE}[Ca^{2+}]$_{nrs}$/dt, are shown in *B* with different colors. The analysis from 0 to ~12 and 18 to ~30 s in *E* were expanded in *C* and *D*, respectively.

regulation were revealed. The model reproduced steady-state activities of the IP$_3$R1 that occur as a consequence of the receptor's allosteric regulation by [Ca^{2+}] and [IP$_3$] (Fig. 1). Using a minimal cell model in which GLP-1-stimulated cAMP production induced an increase of IP$_3$R and SERCA activities, we successfully reconstructed not only the Ca^{2+}- and IP$_3$-induced Ca^{2+} transients (Fig. 3, *B* and *D*) but also oscillatory Ca^{2+} responses initiated by GLP-1. Ca^{2+} transients and Ca^{2+} oscillations could be induced when IP$_3$R and SERCA activities were elevated from basal levels (P_{IP3R} = 13.65 fl/ms and P_{SERCA} = 0.069 amol/ms) to elevated levels (P_{IP3R} = 174.72 fl/ms and P_{SERCA} = 0.23 amol/ms) that are predicted to exist when β-cells are stimulated with GLP-1.

Simulation studies presented here (Fig. 4) suggest that the time courses of the Ca^{2+} transients are dictated by sequential positive and negative feedback regulation in which there is faster activation and slower inhibition of the IP$_3$R by Ca^{2+}. Initiation of the Ca^{2+} transient (CICR) occurs due to positive feedback involving a Ca^{2+}-dependent increase in P_{CaAca} when Ca^{2+} or IP$_3$ activate the IP$_3$R enough so that Ca^{2+} liberation (J_{IP3R} + J_{ERleak}) exceeds its removal from the cytosol (J_{SERCA}+ J_{mleak}). The peak of the Ca^{2+} response is achieved when the J_{IP3R} starts to decline primarily due to an increase in P_{CaIca}, so that J_{efflux} drops below $J_{excretion}$. The rate of change in P_{CaIca} provides a remarkable contribution to the rate of decay in the transient response and to ultimate termination of CICR. Bifurcation analysis also revealed that sequential positive and negative feedback regulation of the IP$_3$R by Ca^{2+} was a crucial property to induce Ca^{2+} oscillations. IE analysis simultaneously disclosed that the key factor to drive and pace Ca^{2+} oscillations was the slower rate of change in P_{CaIca} causing gradual development of Ca^{2+}-dependent inhibition of the IP$_3$R followed by recovery from inhibition (Fig. 6).

Experimental findings compared with stimulation-based studies. Bifurcation analysis presented in Fig. 5, *A–C*, further clarified that the generation of oscillatory Ca^{2+} events was explained by an elevation of Ca$^{2+}{}_{tot}$, as well as IP$_3$R and SERCA activation that reached levels exhibiting stable limit cycles. In true physiological conditions, the increase of Ca$^{2+}{}_{tot}$ occurs during the bursting period when concentrations of glucose rise to stimulatory levels. Simultaneously, IP$_3$R and SERCA activity is increased by GLP-1, as discussed above. Although these fundamental mechanisms underlie rhythmic IP$_3$R-mediated Ca^{2+} mobilization, it must be pointed out that only a few reports exist in which oscillatory Ca^{2+} release was found to occur in β-cells (18, 31–33). The difficulty to demonstrate oscillatory Ca^{2+} events might be attributed to the involvement of multiple cellular factors that must occur in a temporally coincident manner. In other words, any failure in the system that causes an insufficient increase in either IP$_3$R or SERCA activity levels, or Ca$^{2+}{}_{tot}$, will lead to imperfect or unsuccessful generation of IP$_3$R-mediated rhythmic Ca^{2+} mobilization.

Importantly, our analysis verifies that IP$_3$R-mediated Ca^{2+} oscillations can be generated when the cytosolic [IP$_3$] is held constant. This finding is consistent with prior experimental results (1, 34, 44). However, since IP$_3$ is the primary agonist for the IP$_3$R, it is evident that [IP$_3$] is an essential contributing factor to determine the activity level of the IP$_3$R so that it may be modulated by cAMP and [Ca^{2+}]$_i$. It is particularly interesting to note that β-cells express a Ca^{2+}-sensitive phospholipase C (PLC) that might participate in the generation of Ca^{2+} oscillations. It catalyzes hydrolysis of phosphatidylinositol 4,5-bisphosphate (PIP$_2$) to produce IP$_3$ (42), and in fact Ca^{2+}-dependent feedback activation of PLC by Ca^{2+} mobilized from IP$_3$R-regulated Ca^{2+} stores is likely to occur (43). Such a feedback process might impact the shape of Ca^{2+} oscillations, as suggested by De Young and Keizer (10).

Modeling vol$_{nrs}$ reveals insights concerning the importance of Ca^{2+} microdomains. For the simulations reported here, it was assumed that relative to the bulk cytosolic Ca^{2+} concentration ([Ca^{2+}]$_{blk}$), individual microdomains ("nrs" in Fig. 2) of elevated Ca^{2+} concentration ([Ca^{2+}]$_{nrs}$) existed at Ca^{2+} release sites where IP$_3$ receptors were located. Therefore, the resultant steep gradient of [Ca^{2+}] between IP$_3$Rs and the bulk space was mathematically represented by incorporation of Ca^{2+} microdomains into the present model. Since there was no reference that suggests the specific size of Ca^{2+} microdomains in β-cells, vol$_{nrs}$ was assumed to be ~1% of the size of vol$_{blk}$ in this study (vol$_{nrs}$ = 7.73 fl). With this assumption, simulations were successfully performed. However, arbitrarily decreasing Vol$_{nrs}$ in concert with increasing P_{nrsblk} (a parameter that determines the flux of Ca^{2+} from nrs to the blk space) also generated Ca^{2+} transients and oscillations, the time courses and amplitudes of which were similar to those simulated with control parameters (cf. Figs. 3 and 5*Ab*). Thus an interplay between Vol$_{nrs}$ and P_{nrsblk} led to an inability to precisely determine the exact values for these two parameters. Although exact values for vol$_{nrs}$ and P_{nrsblk} were not estimated, our assumption of small microdomains of high [Ca^{2+}] occurring at point sources of Ca^{2+} release ("nrs") was shown to be a valid. Omission of "nrs" from the model led to a situation in which the simulations failed to reconstruct transient and oscillatory Ca^{2+} responses that were previously observed under experimental conditions (i.e., the peak as well as the interval separating the oscillatory Ca^{2+} release events were severely increased, data not shown).

Conclusion. For nearly 30 yr it has been appreciated that the insulin secretagogue action of the GLP-1 is a glucose-dependent phenomenon (28). More specifically, GLP-1 potentiates glucose-stimulated insulin secretion only when levels of glucose are elevated to concentrations that are themselves capable of initiating insulin exocytosis. This glucose-dependent action of GLP-1 is due, at least in part, to synergistic activation of the IP$_3$R by glucose metabolism and the GLP-1/cAMP signaling pathways. When considering the action of glucose, it is established that oxidative glucose metabolism in β-cells generates cytosolic ATP, a nucleotide that increases IP$_3$R Ca^{2+} sensitivity by producing a left-shift of the IP$_3$R open probability (P_o) as a function of the Ca^{2+} concentration relationship (15). Glucose metabolism also promotes Ca^{2+} influx, and the ensuing increase of [Ca^{2+}]$_i$ allows Ca^{2+} to act as a coagonist with IP$_3$ so that it may activate the IP$_3$R. When considering the action of GLP-1, evidence exists for the participation of PKA, a protein kinase that phosphorylates IP$_3$ receptors so that they open more efficiently in response to Ca^{2+} (41). GLP-1 also activates the cAMP sensor Epac2 to stimulate a novel PLCε that promotes protein kinase C (PKC) activation and additional Ca^{2+} mobilization (13). Thus coadministration of glucose and GLP-1 to β-cells leads to cyclic activation of the IP$_3$R with resultant oscillations of [Ca]$_i$ that stimulate insulin exocytosis. This constitutes a novel mechanism of CICR, and as demonstrated by the mathematical simulations reported here, IP$_3$ receptors are considered to be molecular coincidence detectors dually activated by IP$_3$ and Ca^{2+} in a context-specific manner. Elevated glucose metabolism is an essential contributing factor, whereas GLP-1/cAMP renders IP$_3$ receptors fully competent to release Ca^{2+} in response to both IP$_3$ and Ca^{2+}. Although the simulations presented here are clearly relevant to mouse β-cells, our minimal model will eventually need to be expanded to include the participation of other types of intracellular Ca^{2+} release channels. For example, evidence exists that in human and rat β-cells, RYR2-mediated CICR can contribute to processes of ER Ca^{2+} mobilization (7, 20).

GRANTS

Y. Takeda, T. Shimayoshi, and A. Noma acknowledge the support of a Grant-In-Aid for Scientific Research from the Ministry of Education, Culture, Sports, Science and Technology, Japan. G. G. Holz acknowledges the support of the National Institute of Diabetes and Digestive and Kidney Diseases (Grant R01-DK069575) and a Basic Science Research Award (7-12-BS-077) from the American Diabetes Association.

DISCLOSURES

No conflicts of interest, financial or otherwise, are declared by the author(s).

AUTHOR CONTRIBUTIONS

Author contributions: Y.T. and A.N. conception and design of research; Y.T. and A.N. performed experiments; Y.T., T.S., and G.G.H. analyzed data; Y.T., T.S., and G.G.H. interpreted results of experiments; Y.T. and T.S. prepared figures; Y.T. and G.G.H. drafted manuscript; Y.T., T.S., G.G.H., and A.N. edited and revised manuscript; Y.T., T.S., G.G.H., and A.N. approved final version of manuscript.

REFERENCES

1. **Bartlett PJ, Young KW, Nahorski SR, Challiss RA.** Single cell analysis and temporal profiling of agonist-mediated inositol 1,4,5-trisphosphate, Ca^{2+}, diacylglycerol, and protein kinase C signaling using fluorescent biosensors. *J Biol Chem* 280: 21837–21846, 2005.
2. **Bergsten P.** Slow and fast oscillations of cytoplasmic Ca^{2+} in pancreatic islets correspond to pulsatile insulin release. *Am J Physiol Endocrinol Metab* 268: E282–E287, 1995.
3. **Bezprozvanny I, Ehrlich BE.** ATP modulates the function of inositol 1,4,5-trisphosphate-gated channels at two sites. *Neuron* 10: 1175–1184, 1993.
4. **Bird GJ, Oliver KG, Horstman DA, Obie J, Putney JW Jr.** Relationship between the calcium-mobilizing action of inositol 1,4,5-trisphosphate in permeable AR4-2J cells and the estimated levels of inositol 1,4,5-trisphosphate in intact AR4-2J cells. *Biochem J* 273: 541–546, 1991.
5. **Cha CY, Nakamura Y, Himeno Y, Wang J, Fujimoto S, Inagaki N, Earm YE, Noma A.** Ionic mechanisms and Ca^{2+} dynamics underlying the glucose response of pancreatic β-cells: a simulation study. *J Gen Physiol* 138: 21–37, 2011.
6. **Challiss RA, Smith SM, Potter BV, Nahorski SR.** D-[^{35}S(U)]inositol 1,4,5-trisphosphorothioate, a novel radioligand for the inositol 1,4,5-trisphosphate receptor. Complex binding to rat cerebellar membranes. *FEBS Lett* 281: 101–104, 1991.
7. **Chepurny OG, Kelley GG, Dzhura I, Leech CA, Roe MW, Dzhura E, Li X, Schwede F, Genieser HG, Holz GG.** PKA-dependent potentiation of glucose-stimulated insulin secretion by Epac activator 8-pCPT-2′-O-

Me-cAMP-AM in human islets of Langerhans. *Am J Physiol Endocrinol Metab* 298: E622–E633, 2010.

8. **Danoff SK, Supattapone S, Snyder SH.** Characterization of a membrane protein from brain mediating the inhibition of inositol 1,4,5-trisphosphate receptor binding by calcium. *Biochem J* 254: 701–705, 1988.
9. **Dawson AP, Lea EJ, Irvine RF.** Kinetic model of the inositol trisphosphate receptor that shows both steady-state and quantal patterns of Ca^{2+} release from intracellular stores. *Biochem J* 370: 621–629, 2003.
10. **De Young GW, Keizer J.** A single-pool inositol 1,4,5-trisphosphate-receptor-based model for agonist-stimulated oscillations in Ca^{2+} concentration. *Proc Natl Acad Sci USA* 89: 9895–9899, 1992.
11. **Dean PM.** Ultrastructural morphometry of the pancreatic β-cell. *Diabetologia* 9: 115–119, 1973.
12. **Dyachok O, Gylfe E.** Ca^{2+}-induced Ca^{2+} release via inositol 1,4,5-trisphosphate receptors is amplified by protein kinase A and triggers exocytosis in pancreatic beta-cells. *J Biol Chem* 279: 45455–45461, 2004.
13. **Dzhura I, Chepurny OG, Kelley GG, Leech CA, Roe MW, Dzhura E, Afshari P, Malik S, Rindler MJ, Xu X, Lu Y, Smrcka AV, Holz GG.** Epac2-dependent mobilization of intracellular Ca^{2+} by glucagon-like peptide-1 receptor agonist exendin-4 is disrupted in β-cells of phospholipase C-ε knockout mice. *J Physiol* 588: 4871–4889, 2010.
14. **Finch EA, Turner TJ, Goldin SM.** Calcium as a coagonist of inositol 1,4,5-trisphosphate-induced calcium release. *Science* 252: 443–446, 1991.
15. **Foskett JK, White C, Cheung KH, Mak DO.** Inositol trisphosphate receptor Ca^{2+} release channels. *Physiol Rev* 87: 593–658, 2007.
16. **Fraiman D, Dawson SP.** A model of IP$_3$ receptor with a luminal calcium binding site: stochastic simulations and analysis. *Cell Calcium* 35: 403–413, 2004.
17. **Gilon P, Ravier MA, Jonas JC, Henquin JC.** Control mechanisms of the oscillations of insulin secretion in vitro and in vivo. *Diabetes* 51, *Suppl* 1: S144–S151, 2002.
18. **Grapengiesser E, Gylfe E, Hellman B.** Cyclic AMP as a determinant for glucose induction of fast Ca^{2+} oscillations in isolated pancreatic beta-cells. *J Biol Chem* 266: 12207–12210, 1991.
19. **Holz GG, Heart E, Leech CA.** *Synchronizing Ca^{2+} and cAMP oscillations in pancreatic β-cells: a role for glucose metabolism and GLP-1 receptors?* Focus on “Regulation of cAMP dynamics by Ca^{2+} and G protein-coupled receptors in the pancreatic β-cell: a computational approach”. *Am J Physiol Cell Physiol* 294: C4–C6, 2008.
20. **Holz GG, Leech CA, Heller RS, Castonguay M, Habener JF.** cAMP-dependent mobilization of intracellular Ca^{2+} stores by activation of ryanodine receptors in pancreatic beta-cells. A Ca^{2+} signaling system stimulated by the insulinotropic hormone glucagon-like peptide-1-(7–37). *J Biol Chem* 274: 14147–14156, 1999.
21. **Horstman DA, Takemura H, Putney JW Jr. Formation and metabolism of [^{3}H]inositol phosphates in AR42J pancreatoma cells.** Substance P-induced Ca^{2+} mobilization in the apparent absence of inositol 1,4,5-trisphosphate 3-kinase activity. *J Biol Chem* 263: 15297–15303, 1988.
22. **Joseph SK, Rice HL, Williamson JR.** The effect of external calcium and pH on inositol trisphosphate-mediated calcium release from cerebellum microsomal fractions. *Biochem J* 258: 261–265, 1989.
23. **Kaftan EJ, Ehrlich BE, Watras J.** Inositol 1,4,5-trisphosphate (InsP$_3$) and calcium interact to increase the dynamic range of InsP$_3$ receptor-dependent calcium signaling. *J Gen Physiol* 110: 529–538, 1997.
24. **Kang G, Chepurny OG, Holz GG.** cAMP-regulated guanine nucleotide exchange factor II (Epac2) mediates Ca^{2+}-induced Ca^{2+} release in INS-1 pancreatic beta-cells. *J Physiol* 536: 375–385, 2001.
25. **Kang G, Chepurny OG, Rindler MJ, Collis L, Chepurny Z, Li WH, Harbeck M, Roe MW, Holz GG.** A cAMP and Ca^{2+} coincidence detector in support of Ca^{2+}-induced Ca^{2+} release in mouse pancreatic beta cells. *J Physiol* 566: 173–188, 2005.
26. **Kang G, Holz GG.** Amplification of exocytosis by Ca^{2+}-induced Ca^{2+} release in INS-1 pancreatic beta cells. *J Physiol* 546: 175–189, 2003.
27. **Kang G, Joseph JW, Chepurny OG, Monaco M, Wheeler MB, Bos JL, Schwede F, Genieser HG, Holz GG.** Epac-selective cAMP analog 8-pCPT-2′-O-Me-cAMP as a stimulus for Ca^{2+}-induced Ca^{2+} release and exocytosis in pancreatic beta-cells. *J Biol Chem* 278: 8279–8285, 2003.
28. **Kashima Y, Miki T, Shibasaki T, Ozaki N, Miyazaki M, Yano H, Seino S.** Critical role of cAMP-GEFII-Rim2 complex in incretin-potentiated insulin secretion. *J Biol Chem* 276: 46046–46053, 2001.
29. **Lee B, Laychock SG.** Inositol 1,4,5-trisphosphate receptor isoform expression in mouse pancreatic islets: effects of carbachol. *Biochem Pharmacol* 61: 327–336, 2001.
30. **Leech CA, Dzhura I, Chepurny OG, Kang G, Schwede F, Genieser HG, Holz GG.** Molecular physiology of glucagon-like peptide-1 insulin secretagogue action in pancreatic beta cells. *Prog Biophys Mol Biol* 107: 236–247, 2011.
31. **Liu YJ, Grapengiesser E, Gylfe E, Hellman B.** Crosstalk between the cAMP and inositol trisphosphate-signalling pathways in pancreatic beta-cells. *Arch Biochem Biophys* 334: 295–302, 1996.
32. **Liu YJ, Tengholm A, Grapengiesser E, Hellman B, Gylfe E.** Origin of slow and fast oscillations of Ca^{2+} in mouse pancreatic islets. *J Physiol* 508: 471–481, 1998.
33. **MacDonald PE, El-Kholy W, Riedel MJ, Salapatek AM, Light PE, Wheeler MB.** The multiple actions of GLP-1 on the process of glucose-stimulated insulin secretion. *Diabetes* 51, *Suppl* 3: S434–S442, 2002.
34. **Matsu-ura T, Michikawa T, Inoue T, Miyawaki A, Yoshida M, Mikoshiba K.** Cytosolic inositol 1,4,5-trisphosphate dynamics during intracellular calcium oscillations in living cells. *J Cell Biol* 173: 755–765, 2006.
35. **Michikawa T, Hirota J, Kawano S, Hiraoka M, Yamada M, Furuichi T, Mikoshiba K.** Calmodulin mediates calcium-dependent inactivation of the cerebellar type 1 inositol 1,4,5-trisphosphate receptor. *Neuron* 23: 799–808, 1999.
36. **Moraru II, Kaftan EJ, Ehrlich BE, Watras J.** Regulation of type 1 inositol 1,4,5-trisphosphate-gated calcium channels by InsP$_3$ and calcium: simulation of single channel kinetics based on ligand binding and electrophysiological analysis. *J Gen Physiol* 113: 837–849, 1999.
37. **Nadkarni P, Chepurny OG, Holz GG.** Regulation of glucose homeostasis by GLP-1. *Prog Mol Biol Transl Sci* 121: 23–65, 2014.
38. **Santos RM, Rosario LM, Nadal A, Garcia-Sancho J, Soria B, Valdeolmillos M.** Widespread synchronous [Ca^{2+}]$_i$ oscillations due to bursting electrical activity in single pancreatic islets. *Pflügers Arch* 418: 417–422, 1991.
39. **Shimayoshi T, Cha CY, Amano A.** Quantitative decomposition of dynamics of mathematical cell models: method and application to ventricular myocyte models. *PLoS One* 10: e0124970, 2015.
40. **Sienaert I, De SH, Parys JB, Missiaen L, Vanlingen S, Sipma H, Casteels R.** Characterization of a cytosolic and a luminal Ca^{2+} binding site in the type I inositol 1,4,5-trisphosphate receptor. *J Biol Chem* 271: 27005–27012, 1996.
41. **Tang TS, Tu H, Wang Z, Bezprozvanny I.** Modulation of type 1 inositol (1,4,5)-trisphosphate receptor function by protein kinase A and protein phosphatase 1α. *J Neurosci* 23: 403–415, 2003.
42. **Tengholm A, Gylfe E.** Oscillatory control of insulin secretion. *Mol Cell Endocrinol* 297: 58–72, 2009.
43. **Thore S, Dyachok O, Gylfe E, Tengholm A.** Feedback activation of phospholipase C via intracellular mobilization and store-operated influx of Ca^{2+} in insulin-secreting beta-cells. *J Cell Sci* 118: 4463–4471, 2005.
44. **Wakui M, Potter BV, Petersen OH.** Pulsatile intracellular calcium release does not depend on fluctuations in inositol trisphosphate concentration. *Nature* 339: 317–320, 1989.
45. **Worley PF, Baraban JM, Supattapone S, Wilson VS, Snyder SH.** Characterization of inositol trisphosphate receptor binding in brain. Regulation by pH and calcium. *J Biol Chem* 262: 12132–12136, 1987.
46. **Yaekura K, Yada T.** [Ca^{2+}]$_i$-reducing action of cAMP in rat pancreatic beta-cells: involvement of thapsigargin-sensitive stores. *Am J Physiol Cell Physiol* 274: C513–C521, 1998.